Geothermics 110 (2023) 102683

Contents lists available at ScienceDirect

Geothermics

journal homepage: www.elsevier.com/locate/geothermics

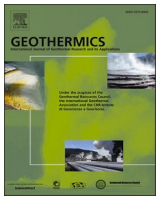

Geomechanical analysis of the geothermal reservoir at San Emidio, Nevada

Ben Jahnke [a,*], Hiroki Sone [a], Hao Guo [a], Chris Sherman [b], Ian Warren [c,1], Corné Kreemer [d], Clifford H. Thurber [a], Kurt L. Feigl [a], The WHOLESCALE Team

[a] University of Wisconsin-Madison, Madison, Wisconsin, United States
[b] Lawrence Berkeley National Laboratory, Berkeley, California, United States
[c] National Renewable Energy Lab, Golden, Colorado, United States
[d] University of Nevada-Reno, Reno, Nevada, United States

ARTICLE INFO

Keywords:
Wholescale
San Emidio
Stress
Stress inversion

ABSTRACT

The WHOLESCALE (Water and Hole Observations Leverage Effective Stress Calculations and Lessen Expenses) project is aiming to simulate the spatial distribution and temporal evolution of stress throughout the geothermal system at San Emidio, Nevada, United States, via a thermo-hydro-mechanical reservoir model. Focal mechanisms for microseismic events during a temporary shutdown of the geothermal power plant in 2016 were analyzed through linear stress-inversion methods to infer the *in-situ* reservoir stress state. This analysis was supplemented by other geophysical and geological data, including focal mechanisms from regional earthquakes, slickenlines on exposed fracture surfaces, wellbore stress indicators observed in the surrounding region, and secular strain rate measurements. From the inferences of *in-situ* reservoir stress, 78 different realizations of stress models were generated over reasonable ranges for the values of maximum compressive horizontal stress (S_{Hmax}) azimuth and ratios of principal stress magnitudes. Evaluation of slip tendencies on fault planes determined for the microseismic events for each realization of the initial stress model suggests the reservoir stress state as transtensional with an S_{Hmax} azimuth between N and N30°E.

1. Introduction

As described by Feigl et al. (2022), the WHOLESCALE project seeks to construct a reservoir-scale stress model that simulates the spatial distribution and temporal evolution of stress in and around the geothermal system at San Emidio, Nevada, United States. Knowledge of the orientations and magnitudes of the principal stresses at reservoir depths is necessary to predict the orientations of mechanically active and hydraulically conductive fractures that can transport fluids and heat, and establish fluid pressure thresholds for fracture creation and reactivation. This information allows plant operators to locate and engineer geothermal production and injection wells for efficient and sustainable energy production, design hydraulic stimulations to increase reservoir permeability, and inform coupled thermo-hydro-mechanical-chemical models for long-term reservoir management. When combined with information on the orientation of potentially active faults, in-situ stress data can also help evaluate and mitigate risks associated with induced seismicity.

This study used geophysical and geological data to constrain the orientation and magnitudes of stress that are used as initial conditions in the multi-physics stress model developed for the geothermal reservoir at San Emidio. Density logs and measurements of formation tops (Folsom et al., 2020) from wellbores at San Emidio were used to estimate vertical stress magnitudes, and the orientation and relative magnitudes of principal stresses within the reservoir were constrained using microseismic events that occured during a geothermal plant shut down in 2016 where injection and production ceased. Slickenlines on faults in outcrop exposures were also used to constrain principal stress directions and relative stress magnitudes.

1.1. History of San Emidio

In the late 1970s, early exploration of the San Emidio region began by several companies conducting surveys and drilling wells (Folsom et al., 2020). This early exploration defined a shallow geothermal reservoir, with temperatures reaching ~134 °C (Matlick, 1995). In the mid to late 1980s, the Empire power plant drilled more than a dozen

* Corresponding author.
E-mail address: bjahnke3@wisc.edu (B. Jahnke).
[1] Now at Zanskar Geothermal & Minerals, Inc.

https://doi.org/10.1016/j.geothermics.2023.102683
Received 26 June 2022; Received in revised form 28 October 2022; Accepted 18 February 2023
Available online 6 March 2023

List of symbols

S_V	total vertical stress
S_{Hmax}	total maximum horizontal stress
S_{hmin}	total minimum horizontal stress
$\rho(z)$	rock density as a function of depth
g	gravitational acceleration
z	depth below the surface
σ_1	maximum effective principal stress
σ_2	intermediate effective principal stress
σ_3	minimum effective principal stress
S_1	maximum total stress
S_3	minimum total stress
P_p	pore fluid pressure
μ	coefficient of rock friction
T_S	slip tendency
τ	shear traction
σ_n	normal traction
I	fault instability
R	shape ratio

wells, targeting this shallow reservoir. In 1987, the AMOR II Corp commissioned a 3.6 MW binary power plant which used the shallow wells. In the early 1990s, Empire drilled deeper wells discovering a deeper reservoir. In 2008, U.S. Geothermal acquired the Empire power plant and began to maximize production from the geothermal field. In 2012, a 14.7 MW power plant was commissioned. This resulted in the drilling of exploration wells which defined a deeper, hotter reservoir, with temperatures reaching 154 – 161 °C. In 2016, exploration wells were deepened such that four wells encountered commercially viable temperatures and permeability at depths of 560 – 670m. The current gross and net generation at San Emidio are 13.9 MW and 10.3 MW, respectively.

1.2. Reservoir geology

The geothermal reservoir is located in the San Emidio desert of northwestern Nevada, United States. The reservoir is in a fractured rock volume with a network of primarily westward dipping normal faults (Fig. 1). Geologic units composing the reservoir include playa deposits (Tps), alluvium (Qal), Silicified and acid-sulfate altered alluvium (Qas), Miocene to Pliocene sedimentary rocks (Ts), silicified sedimentary rocks (Tss), porphyritic basaltic andesite (Tpb, Tpb'), tuffaceous and volcaniclastic rocks (Tvu, Tptsu), and metasediments – phyllite (TrJn). A geologic map has been published by Rhodes (2011) and a complete description of the mapped geologic units has been published in Rhodes et al. (2011).

The shallower and cooler parts of the reservoir are composed of poorly lithified sedimentary sequences, whereas the deeper and hotter parts of the reservoir are composed of low porosity volcanic and metamorphic rocks. Due to the low porosity in the deeper and hotter rocks, fluid transport is concentrated in faults and fractures.

1.3. Regional stress indicators

Stress indicators within a ~175km radius surrounding San Emidio were considered to reflect the background regional tectonic stress (Fig. 2). The regional azimuth of greatest principal stress S_{Hmax}, was obtained from the World Stress Map (Heidbach et al., 2018) and wellbore indicators in the form of breakouts and drilling induced tensile fractures observed in nearby geothermal fields. Stress indicators from the World Stress Map primarily come from earthquake focal mechanisms, which indicated a maximum compressive horizontal stress azimuth near N10°E in a normal or strike-slip stress regime. Wellbore stress indicators from nearby geothermal fields at Astor Pass (Siler et al., 2016), Dixie Valley (Hickman et al., 1998), and Desert Peak (Davatzes and Hickman, 2009; Hickman and Davatzes, 2010) indicated S_{Hmax} azimuths of N3°E±12°, N33°E±10°, and N24°E±17°, respectively. Additionally, the faulting regimes at Astor Pass, Dixie Valley, and Desert Peak are strike-slip, normal, and normal, respectively. Although not an indicator of stress, the direction of maximum contractional secular strain rate is N3°E at San Emidio (Kreemer et al., 2014) indicating that the background regional tectonic stress and strain rate directions appear to be subparallel.

1.4. Microseismicity from 2016 geothermal power plant shut down

The geothermal power plant at San Emidio is composed of a system of injection and production wells that circulate water through faults and fractures within the reservoir. During normal plant operations when water is being cycled through the reservoir, the groundwater levels around the production wells are inferred to form a cone of depression, as described by the Theis equation (Theis, 1940), and pore pressure around the production wells is relatively low. However, during a plant shutdown, injection into the injection wells and pumping out of the production wells is stopped. This causes fluid levels around the production wells to recover which results in a local increase in pore fluid pressure. As pore fluid pressures rise, the effective normal stresses decrease, thus increasing the tendency of fault slip and making microseismic events more likely.

In December of 2016, injection and production pumping at the geothermal power plant ceased for about 20 h, which stopped all fluid flow into and out of the reservoir. Pore fluid pressures were estimated to increase on the order of tens of kPa (Feigl et al., 2022). Presumably, as a response to the increase in pore fluid pressure, a total of 122 microseismic events were recorded. The configuration of the seismic network deployed in 2016 is shown in Warren et al. (2019). Such small changes in pore fluid pressures resulting in microseismicity indicates that the reservoir is critically stressed (Zoback and Harjes, 1997). Focal mechanisms were determined for 31 of the events (Guo et al., 2022; "Seismic Analysis of Induced Microseismicity Due to Pumping Cessation at the San Emidio Geothermal Field, Nevada" unpublished manuscript by Hao Guo et al.) (Fig. 3). Using the events with focal mechanism solutions, stress inversions were performed to infer the reservoir stress state.

2. Methods

2.1. Frictional constraints on initial stress model

The vertical and horizontal stress magnitudes were approximated using known rock densities and formation tops from San Emidio well logs and using frictional constraints on the relative magnitudes of *in-situ* principal stresses. The total vertical stress, S_V, equals the lithostatic stress from the overlying rock:

$$S_V = \int_0^z \rho(z) g dz \tag{1}$$

where $\rho(z)$ is the rock density as a function of depth, g is gravitational acceleration, and z is depth below the surface (Jaeger and Cook, 1971). Formation tops were estimated from log data, and densities of the formations were obtained from previous studies (Folsom et al., 2020).

Bounds on the magnitudes of the horizontal principal stresses were obtained assuming that differential stresses are controlled by the frictional strength of optimally oriented faults:

$$\frac{\sigma_1}{\sigma_3} = \frac{S_1 - P_p}{S_3 - P_p} \leq \left[\left(\mu^2 + 1\right)^{\frac{1}{2}} + \mu\right]^2 \tag{2}$$

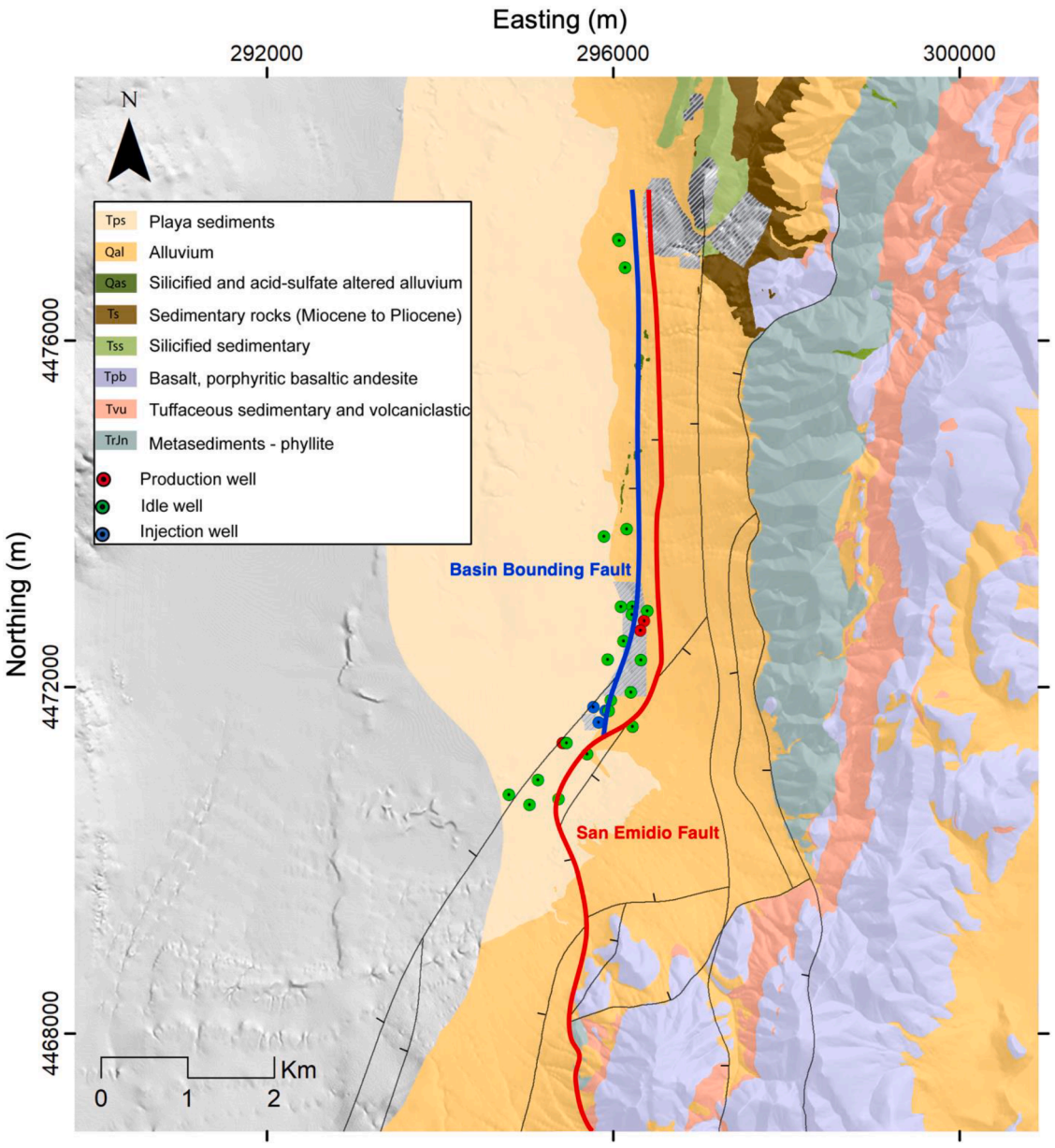

Fig. 1. Geologic map of San Emidio. Tick marks on fault traces indicate dip direction. Blue, red, and green circles indicate injection, production, and observation wells, respectively. For complete description of geologic units, see Rhodes et al. (2011).

where σ_1 is the maximum effective principal stress, σ_3 is the minimum effective principal stress, S_1 is the maximum total stress, S_3 is the minimum total stress, P_p is the pore fluid pressure, μ is the coefficient of rock friction (Zoback, 2007), and compressive stresses are reckoned positive. A hydrostatic pore pressure gradient with a water table at the surface was assumed. A coefficient of friction of $\mu = 0.6$ and zero cohesion was assumed (Byerlee, 1978). As discussed below, profiles of the least and greatest horizontal principal stresses, S_{hmin} and S_{Hmax}, respectively, were generated for 13 different relative magnitudes of vertical and horizontal stresses (stress ratios) spanning critically stressed normal to transpressional regimes.

2.2. Stress models

The reservoir stress model (Fig. 4) is generated using GEOSX, an open-source, multi-physics reservoir simulator which computes the 3D stress tensor within a meshed volume (Settgast et al., 2018). A geologic model (Folsom et al., 2020) was used to obtain vertical stresses throughout the model. Stress ratios from Eq. (2) and ranges of regional S_{Hmax} azimuths (Fig. 2) provided estimates of horizontal principal stress magnitudes and orientations. The initial estimates of vertical and horizontal stresses within the domain were then allowed to equilibrate with adjacent elements to generate a mechanically equilibrated stress model.

Motivated by the findings from the regional stress indicators (Fig. 2), we generated different realizations of the initial stress model for a range of six different S_{Hmax} azimuths and 13 stress ratios. A total of 78 (13×6) different realizations of initial stress models were generated (Fig. 5). A hydrostatic pore pressure model was incorporated with the 78 realizations of initial stress models to calculate the effective stresses. Since microseismic events were induced by pore pressure changes on the order of tens of kPa, the stress states in each realization of the initial stress model were assumed to be critically stressed.

2.3. Slip tendency

To calculate the propensity for slip on faults identified through

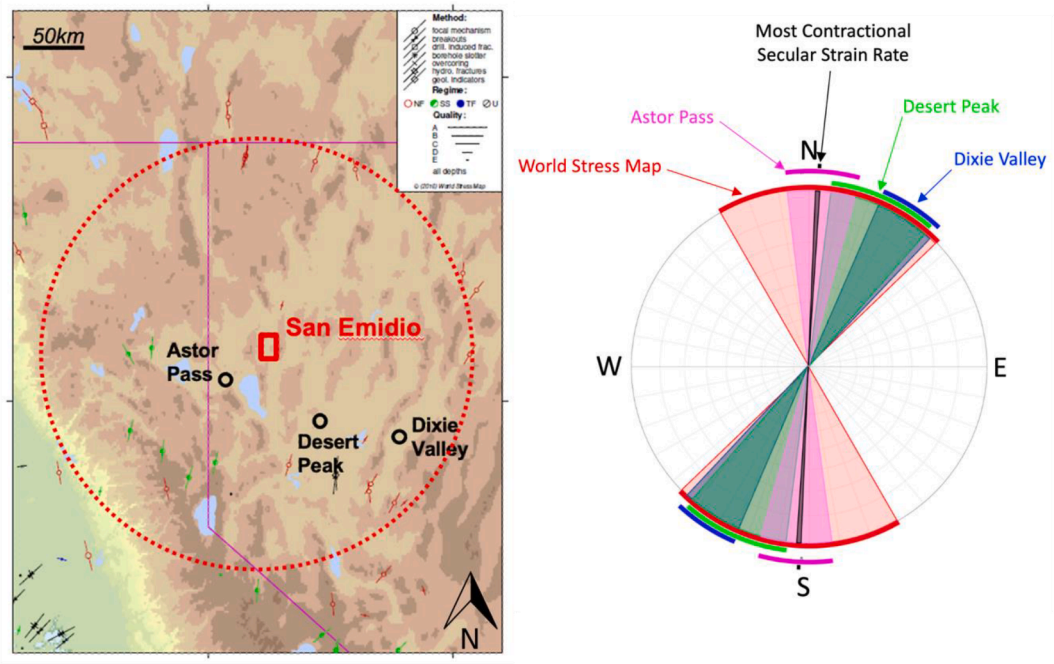

Fig. 2. (Left) World Stress Map with locations of stress indicators within a ~175 km radius around San Emidio. Figure modified from Heidbach et al. (2018). (Right) Summary of regional observations of S_{Hmax} azimuths.

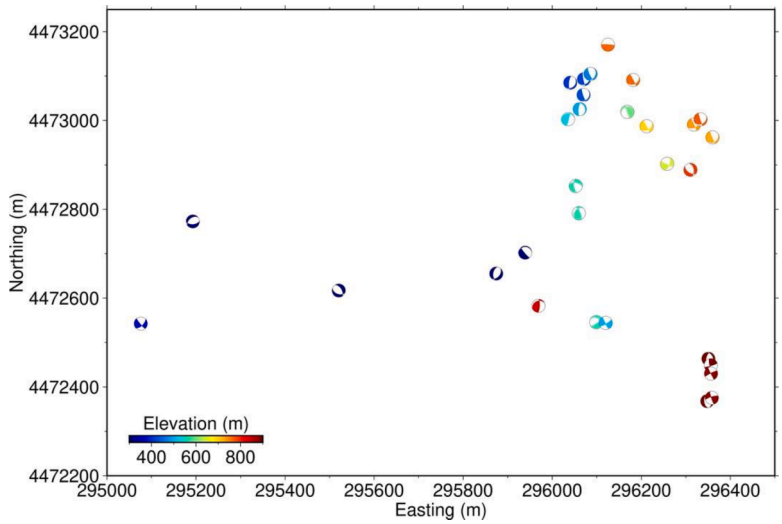

Fig. 3. Focal mechanism solutions from microsesimic events during the 2016 plant shut down. Elevation is meters above mean sea level. 30 of the 31 focal mechanisms shown to maximize visibility of focal planes. See Fig. 12 for all microsesimic event locations.

geologic mapping, geophysical imaging and seismic observations at San Emidio, slip tendency was calculated on the pre-existing fault surfaces within the stress model and the inferred slip planes of the microseismic events from the 2016 plant shut down. Slip tendency is defined by the following equation:

$$T_S = \frac{\tau}{\sigma_n - P_p} \tag{3}$$

where τ and σ_n are the shear and normal tractions on a fault plane (Morris et al., 1996). Slip will occur on a fault when the shear traction reaches the frictional resistance to sliding.

Faults within the stress model were defined by a set of coordinates located on the fault surfaces estimated from past geophysical investigations and wells (Folsom et al., 2020). The coordinates were triangulated to form fault patches representing the 3D fault structure. For each of the 78 realizations of the initial stress model, the stress tensor was interpolated at the center of each fault patch. Then, the normal and shear tractions and pore fluid pressure were determined at the center of each fault patch for subsequent slip tendency calculation.

2.4. Stress inversion

To estimate the *in-situ* reservoir stresses, focal mechanism solutions obtained from the 2016 geothermal plant shut down were used to perform linear stress inversions (Michael, 1984). Stress inversions use multiple fault slip data to determine the stress state that minimizes the difference between fault slip vectors and the direction of maximum shear traction on each fault plane.

Since focal mechanisms do not explicitly differentiate between the

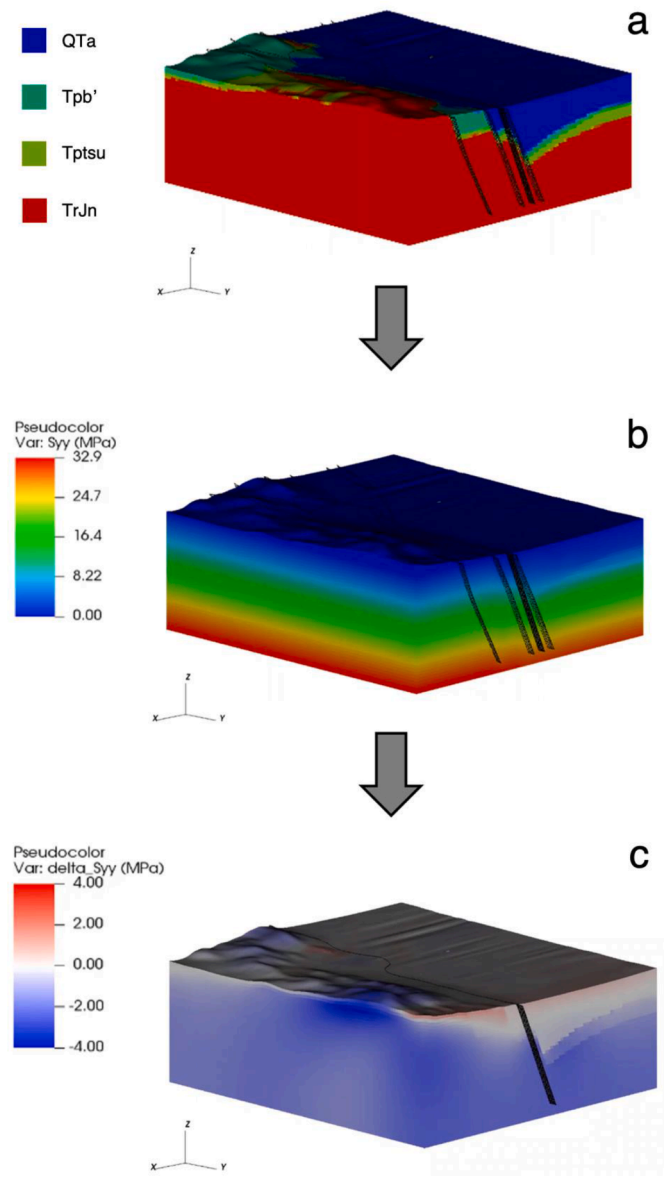

Fig. 4. Generation of initial stress model. (a) Depth-dependent vertical stress calculated from a density model. (b) Maximum and minimum horizontal stresses are assigned based on the chosen stress ratio. (c) Body forces in the model are equilibrated via an implicit solver, producing the initial stress model.

auxiliary and slip plane, an iterative joint inversion (Vavryčuk, 2014) was performed on the focal mechanism data to infer the stress state using the nodal planes closest to the failure state. To differentiate between the fault plane and auxiliary plane, the iterative joint inversion introduces the fault instability, I, which indicates how close to failure a nodal plane is within a stress state. An optimally oriented fault will have a fault instability of $I = 1$, indicating that the fault is unstable, whereas all other faults will have a fault instability of $0 \leq I < 1$. Faults with a fault instability closer to 0 indicate more stable faults.

Each iterative joint inversion begins with a selection of nodal planes from each focal mechanism (Fig. 6). Then, a linear stress inversion is performed using the nodal planes. The fault instability is evaluated for all nodal planes, and the nodal planes from each focal mechanism are identified. If the combination of most unstable nodal planes changed from the previous inversion, then a subsequent linear stress inversion is performed using the most unstable nodal planes from each focal mechanism. The fault instability is evaluated again on each nodal plane from each focal mechanism. This process is iterated until the combination of most unstable nodal planes remains unchanged after each inversion. The final set of nodal planes is then inferred to describe the slip planes of the focal mechanisms. The converged stress state describing the nodal planes with greatest fault instability may depend on the initial selection of nodal planes.

The average misfit angle was determined for each stress inversion. The misfit angle is the angle between the fault slip vectors and orientation of maximum shear traction defined by the inferred stress state on each fault plane. The misfit angle is a metric that describes how well the inferred stress state describes the fault slip data. A small misfit angle indicates an inferred stress state that fits the fault slip data well.

The shape ratio, R, is also determined for each stress inversion:

$$R = \frac{\sigma_1 - \sigma_2}{\sigma_1 - \sigma_3} \tag{4}$$

where σ_1, σ_2, and σ_3, are the magnitudes of the effective principal stresses. Shape ratios range between 0 and 1. A shape ratio near 0 or 1 indicates a stress state with two of the three principal stresses close in magnitude.

3. Results

3.1. Stress profiles

Stress profiles were estimated for 22 of the wells at San Emidio. An example of the stress profiles from the deepest well in the reservoir, Kosmos 1–9, is shown in Fig. 7. The Kosmos 1–9 well reaches a maximum depth of 1636m and penetrates three formations: QTa, Tpb', and TrJn. The stress profile in Fig. 7 is generated for a transtensional stress regime, with a stress ratio $R = 0$ (stress ratio #5 in Fig. 6) At the bottom of Kosmos 1–9, the magnitudes of total vertical stress, maximum horizontal stress, and minimum horizontal stresses were estimated to be 39.3MPa, 39.3MPa, and 23.5MPa, respectively (Fig. 7). GEOSX calculated vertical stress profiles for each choice of S_{Hmax} azimuth and stress ratios to generate the 78 realizations of the initial stress model.

3.2. Slip tendency

Slip tendencies were calculated on the surfaces of the two known large-scale faults included in the model, and on the inferred slip planes of microseismic events from the 2016 plant shut down. Previous mapping had identified faults in the reservoir (Folsom et al., 2020), and the microseismicity from the 2016 shutdown was mostly contained between two faults, the San Emidio (SE) and Basin Bounding (BB) faults (Fig. 1). Slip tendencies on the model SE (Fig. 8) and BB faults (Fig. 9) were determined for each of the 78 realizations of the initial stress model.

As seen in Figs. 8 and 9, each realization of the initial stress model produced high slip tendencies at the shallowest portion of the fault plane. This is caused by high horizontal stresses close to the surface which are enhanced in magnitude by the topography of the mountain range to the east (Fig. 1) when the linear elastic numerical models reach static equilibrium. However, because the vertical stress approaches zero at the surface, this results in inflated slip tendency values close to the surface. In reality, such high differential stress cannot be sustained by the shallow unconsolidated sediments and slip tendencies should not be as high as predicted in the elastic model we employed. Therefore, the high values of slip tendency within about 300m of the surface should be ignored.

As described above, the most unstable nodal plane, or inferred slip plane, was inferred from the iterative stress inversion from focal mechanisms. Slip tendencies were calculated on the inferred slip planes from the iterative stress inversion which used all 31 focal mechanisms. For each of the 78 realizations of the initial stress model, the slip tendencies were averaged amongst all 31 inferred slip planes (Fig. 10). The highest average slip tendency on the inferred slip planes was 0.40 in

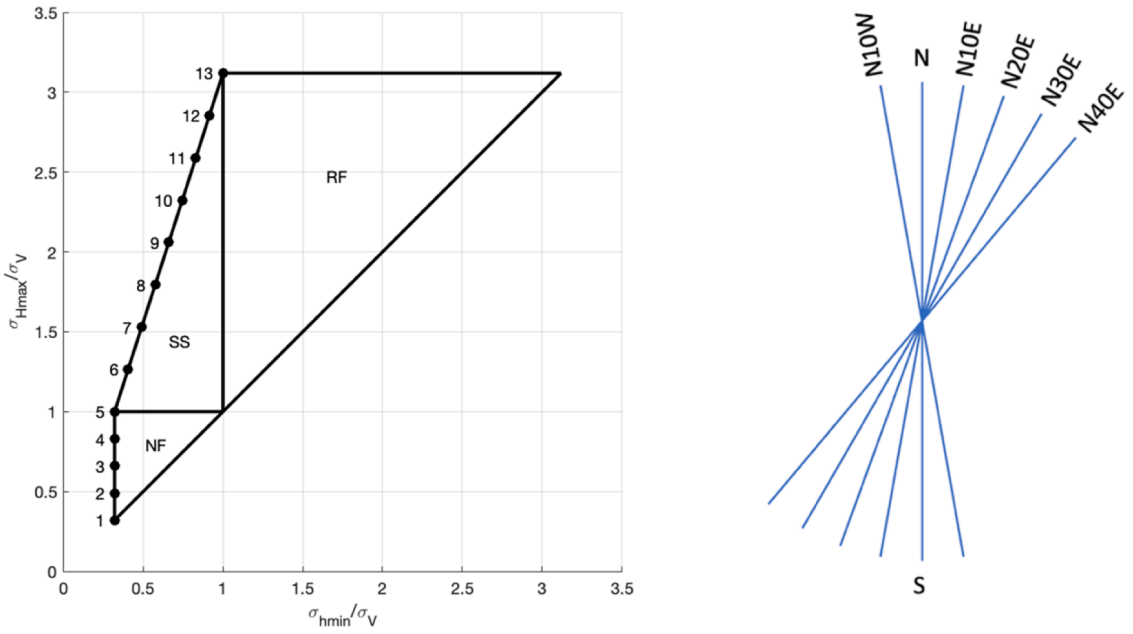

Fig. 5. (Left) Relative magnitudes of effective vertical, maximum horizontal, and minimum horizontal stresses, referred to as stress ratio numbers. (Right) Azimuths of S_{Hmax} (see Fig. 2) were used to generate the 78 different realizations of the initial stress model.

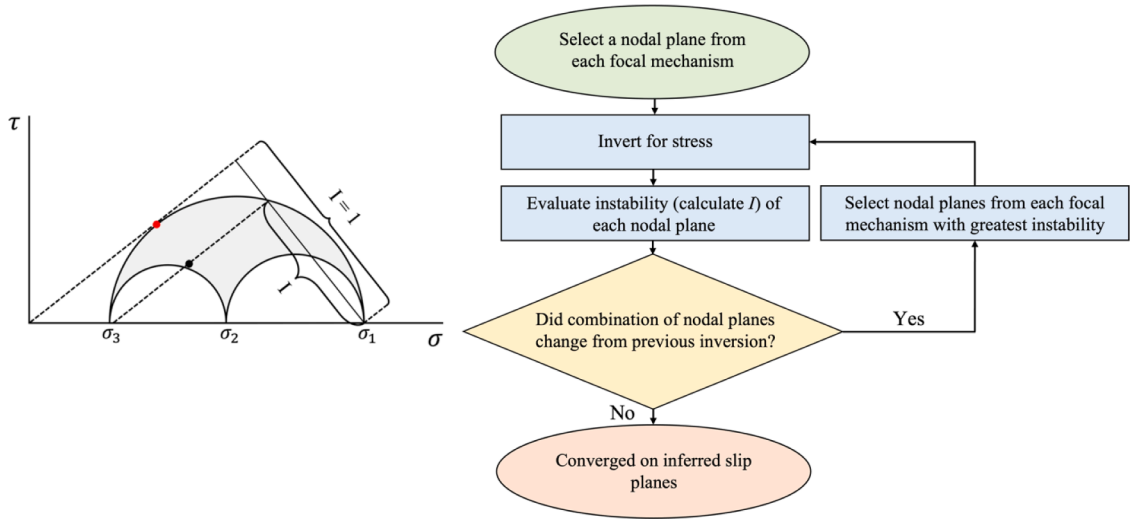

Fig. 6. (Left) Fault stability represented in a Mohr diagram. The red dot indicates the normal and shear tractions on the optimally oriented fault plane with fault instability $I = 1$. The black dot indicates the normal and shear tractions on an arbitrarily oriented fault with instability I. Figure modified form Vavryčuk (2014). (Right) Flowchart describing the procedure used in the iterative joint inversion.

stress models within a transtensional stress regime (equal magnitudes of S_{Hmax} and S_V, stresses critical for normal or strike-slip faulting) and an S_{Hmax} azimuth of N to N10°E.

3.3. Seismological and geologic constraints on stress directions and relative magnitudes

3.3.1. Focal mechanisms

The overall reservoir stress state was inferred using all the focal mechanisms from the 2016 geothermal plant shut down. Following the iterative joint inversion method (Vavryčuk, 2014), the inferred stress state indicated a normal faulting regime, with σ_1 nearly vertical, σ_2 nearly horizontal oriented north-south, and σ_3 nearly horizontal oriented east-west (Fig. 11). The misfit angle was 39° ± 37° degrees, and the stress ratio, R, was 0.64.

To attempt to characterize the reservoir stress heterogeneity in space and time, the 31 focal mechanisms were clustered into spatial and temporal groups (Fig. 12). Spatially clustered focal mechanisms were clustered based on hypocenter location, and sense of slip. Temporally clustered focal mechanisms were clustered based on their occurrence time during the shut down. In total, five spatial clusters and three temporal clusters were formed. The HASH program (Hardebeck & Shearer, 2008) was used to recover the focal mechanisms (Guo et al., 2022). The qualities of the focal mechanisms in each cluster are indicated in Table 1.

Iterative joint inversions were performed on the spatially clustered focal mechanisms (Fig. 13). Independent of the initial choices of nodal planes, clusters S1, S3, and S4 converged into a single inferred stress state. However, the inferred stress states of clusters S2 and S5 showed a dependence on the initial combination of nodal planes used in the

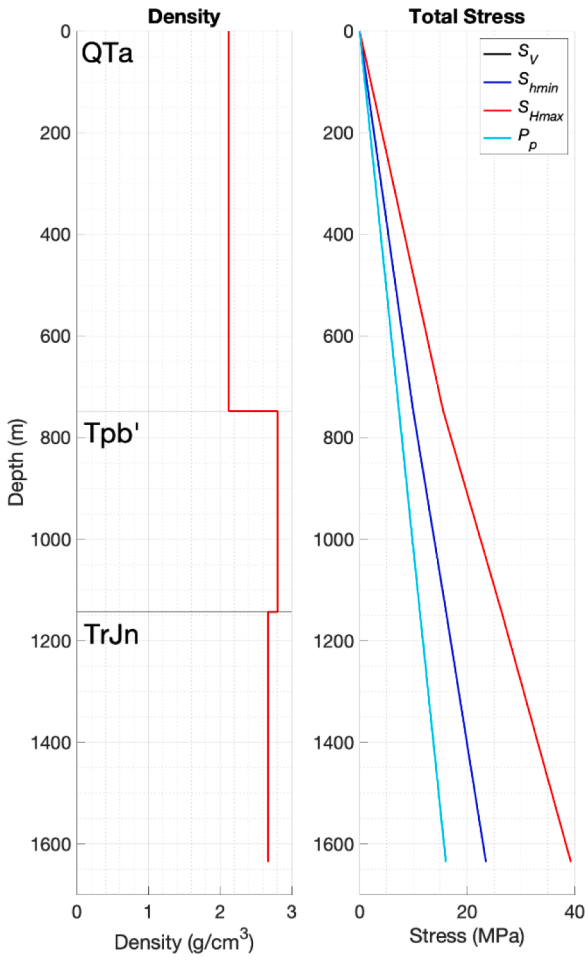

Fig. 7. (Left) Density and (Right) estimated total stress profiles for the Kosmos 1–9 well. S_{Hmax} and S_V are assumed equal in magnitude, corresponding to a transitional normal faulting to strike-slip stress regime. Thus, only S_{Hmax} is shown.

iterative joint inversion. σ_1 is oriented nearly vertical for all spatial clusters except for S4 where σ_2 is the principal stress oriented nearest vertical. There is some variance in the inferred σ_2 orientation depending on the spatial cluster. Although the inferred σ_2 orientations of S1, S3, and S5 are not completely horizontal, their trends are consistent with observed regional S_{Hmax} azimuths. S2 contains one possible inferred stress state with σ_2 oriented nearly horizontal, with a trend consistent with the regional S_{Hmax} azimuth. However, in S2 there is one possible stress state with σ_2 oriented nearly horizontal with a trend at the margin of observed regional SHmax azimuths, and another possible inferred stress state with σ_2 oriented nearly horizontal, but with a trend completely inconsistent with observed regional SHmax azimuths.

The shape ratios are relatively high for two of the three inferred stress states for S2, thus the magnitude of S_{Hmax} and S_{hmin} are close to each other. The inconsistencies between the numerous converged stress states from S2, resulting from the difference in initial choices of the nodal planes, and relatively high average misfit angles suggest that a single stress state cannot be inferred to explain the occurrence of events in S2. The same could be said for cluster S5 which also had a relatively high average misfit angle and multiple converged stress states.

The inferred stress states of all temporal clusters showed a dependence on the initial combination of nodal planes used to start the stress inversions (Fig. 13). σ_1 is oriented nearly vertical for all temporal clusters. There is some variance of the inferred σ_2 orientation depending on the temporal cluster. The inferred σ_2 orientations of T1 are nearly horizontal, but with trends inconsistent with observed regional S_{Hmax} azimuths and clustered in an east-west to Northwest/Southeast orientation. However, the average misfit angles are relatively large, thus the results are either unreliable, or a single stress state may not explain the T1 cluster events. The inferred σ_3 orientations of T1 are more consistent with the regional S_{Hmax} azimuths. Although the inferred σ_2 orientations of T2 and T3 are not completely horizontal, their trends are within the range of observed regional S_{Hmax} azimuths.

The fit of the inferred stress states was evaluated using a single-sample variance test. The misfit angles for each inferred slip plane were normalized using the uncertainty of the focal mechanism orientations. The null hypothesis being tested stated that the normalized misfit angles come from a normal distribution with a variance of 1.0. If the null hypothesis failed to be rejected, that indicated that the variance of the normalized misfits of the nodal planes for the inferred stress state was within the uncertainty of the data. This indicates that a single stress state explains all events. If the null hypothesis was rejected, that

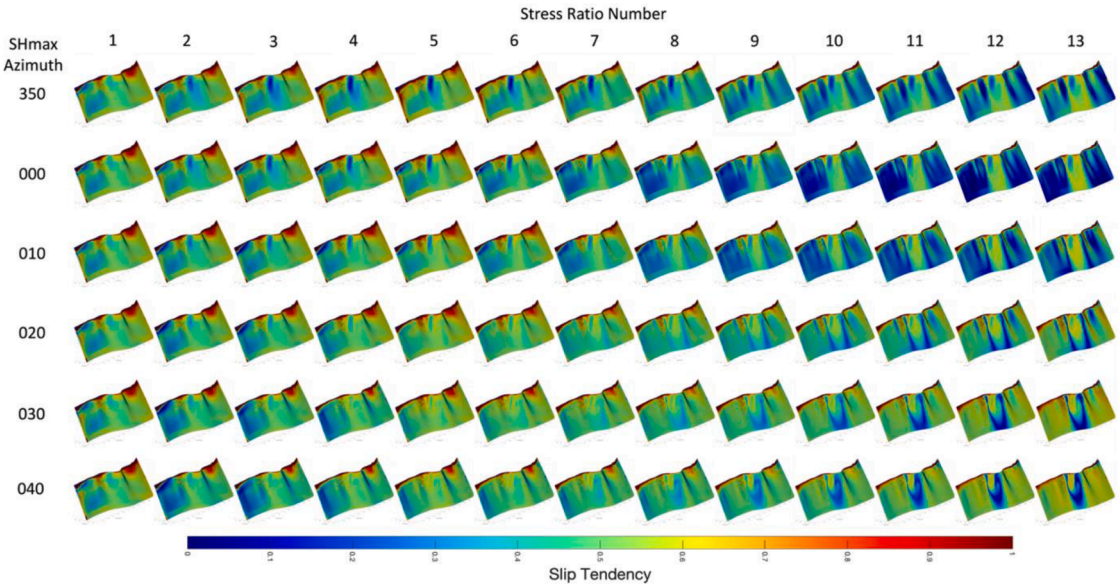

Fig. 8. Values of slip tendency calculated on the SE fault for each stress model realization.

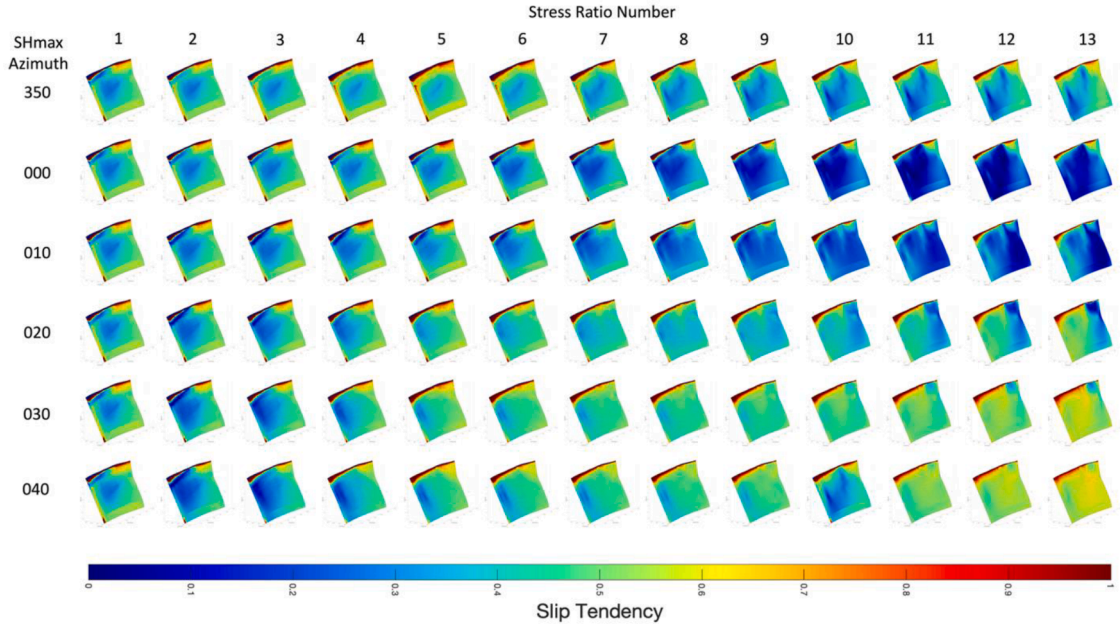

Fig. 9. Values of slip tendency calculated on the BB fault for each stress model realization.

Stress Ratio Number

S_{Hmax} Azimuth	1	2	3	4	5	6	7	8	9	10	11	12	13
350	0.30	0.31	0.32	0.34	0.36	0.35	0.33	0.30	0.29	0.27	0.26	0.25	0.25
0	0.30	0.32	0.35	0.38	0.40	0.38	0.37	0.35	0.34	0.32	0.31	0.30	0.30
10	0.30	0.32	0.35	0.37	0.40	0.38	0.37	0.36	0.34	0.33	0.32	0.31	0.31
20	0.30	0.31	0.32	0.34	0.36	0.35	0.33	0.32	0.32	0.31	0.30	0.29	0.30
30	0.30	0.29	0.28	0.29	0.30	0.29	0.28	0.27	0.27	0.26	0.26	0.27	0.28
40	0.30	0.27	0.25	0.24	0.24	0.23	0.22	0.22	0.21	0.21	0.21	0.22	0.24

Fig. 10. Average slip tendency on the inferred slip planes of the focal mechanisms from the microsesimic events for the 78 realizations of the initial stress model.

indicated that the variance of the normalized misfits of the nodal planes for the inferred stress state was not within the uncertainty of the data. That could indicate that there was not enough data or that the cluster of nodal planes is not described by a single stress state.

The null hypothesis was rejected for the inferred stress states for spatial cluster 3 (S3), temporal cluster 2 (T2), and temporal cluster (T3). This may suggest that the focal mechanisms in each of these clusters could have resulted from more than one stress state within the cluster. However, given the small number of focal mechanisms, we did not attempt to further subdivide the clusters. Cluster S3 in particular falls along a remarkably linear trend (Fig. 12), suggesting events occurring along the same fault plane. This would cause the focal mechanisms to be similar. However, given the consistency with the regional stress, we think the inferred stress state still reflects the *in-situ* stress state.

3.3.2. *Slickenlines*

Kinematic indicators in the form of slickenlines on outcropping fault surfaces in the hills adjacent to the San Emidio power plant (Rhodes, 2011) were used for a stress inversion. The age of the slickenlines is estimated to be ~14 Ma or younger based on $^{40}Ar/^{39}Ar$ geochronologic analysis and structural data of the faulted strata (Rhodes, 2011). A linear stress inversion (Michael, 1984) was performed on the 27 slickenlines. The inferred stress state indicated a normal faulting regime with σ_1 nearly vertical, σ_2 nearly horizontal oriented N20°E, and σ_3 nearly horizontal oriented N70°W, consistent with previous basin and range paleostress analyses (Zoback, 1989). The misfit angle was 19° ± 14° degrees, and the stress ratio, *R*, was 0.80.

3.3.3. *Coefficient of friction sensitivity analysis*

To evaluate the sensitivity of the inferred stress state to the coefficient of friction used in each iterative stress inversion, stress inversions using all 31 focal mechanisms from the 2016 plant shutdown were performed using values of the friction coefficient ranging between 0.1 and 1 with a step size of 0.1 (Fig. A1). For coefficient of friction values 0.5 and greater, the inferred stress states were nearly all the same. The inferred stress states indicated a normal faulting regime, with σ_1 nearly vertical, σ_2 nearly horizontal oriented north-south, and σ_3 nearly horizontal oriented east-west. For coefficient of friction values 0.4 and lower, there was more scatter in possible inferred stress states. Overall, the inferred stress states were in good agreement with the iterative stress inversion result (Fig. 11): a normal faulting regime, with σ_1 nearly vertical, σ_2 nearly horizontal oriented north-south, and σ_3 nearly horizontal oriented east-west.

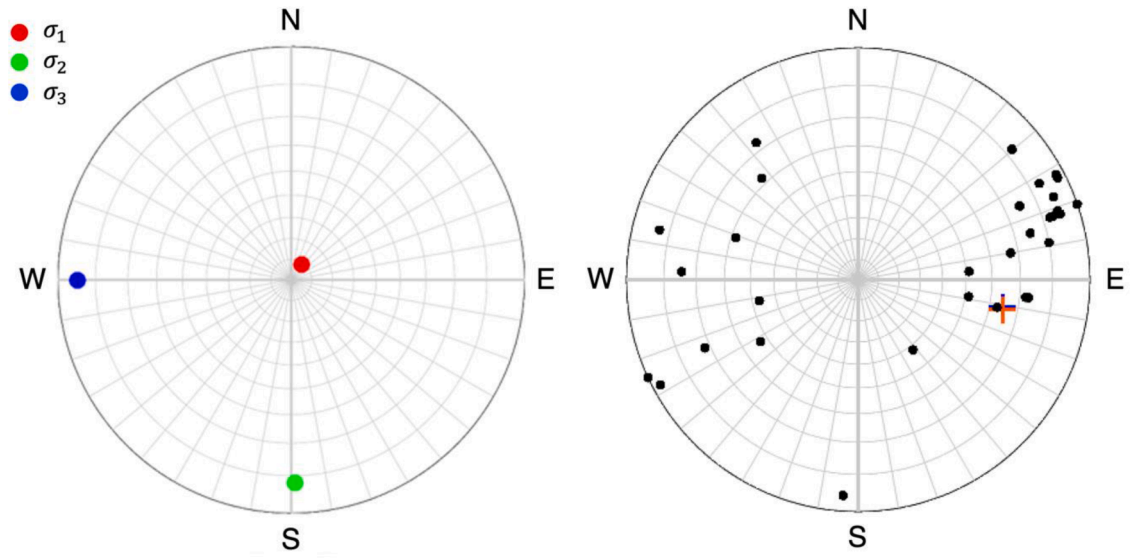

Fig. 11. (Left) Lower hemisphere polar plots with the inferred principal stress directions from iterative stress inversion (Vavryčuk, 2014) using all focal mechanisms. The red, green, and blue markers correspond to the inferred directions of $\boldsymbol{\sigma}_1$, $\boldsymbol{\sigma}_2$, and $\boldsymbol{\sigma}_3$, respectively. (Right) Poles to inferred slip planes from stress inversion using all events are indicated by black circles. Colored crosses indicate the averaged poles to model fault surfaces (blue = Basin Bounding, red = San Emidio).

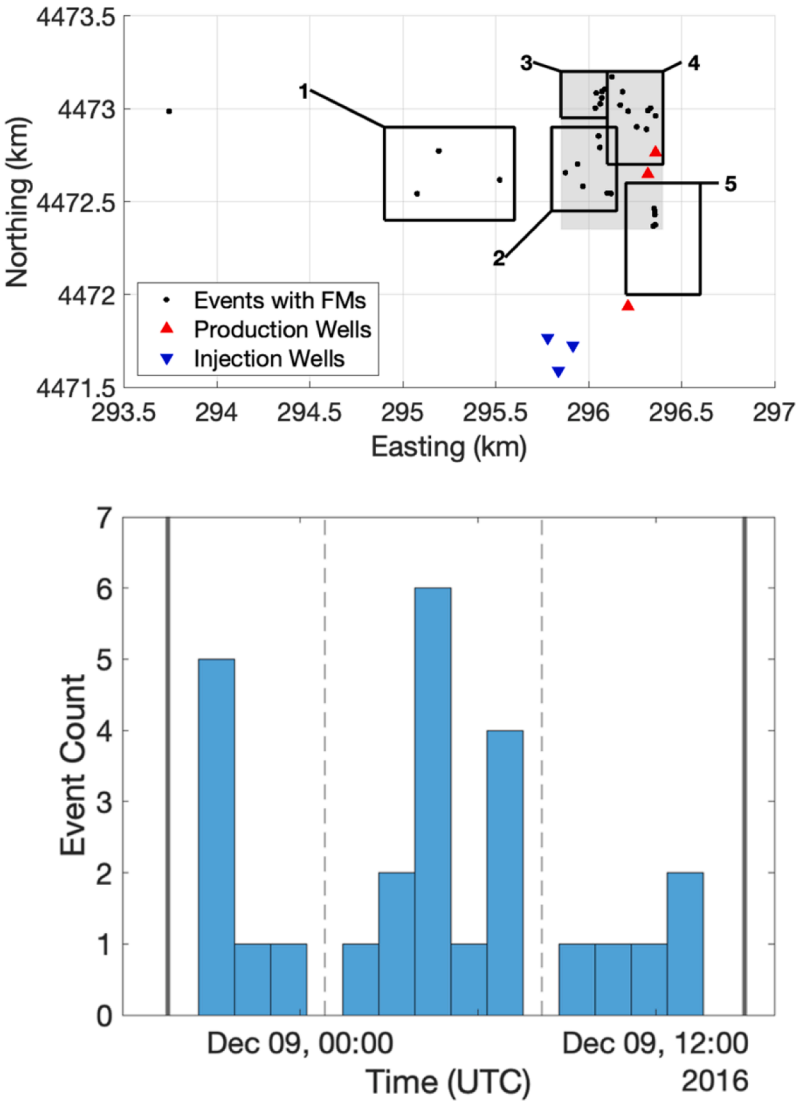

Fig. 12. (Top) Spatial clusters and (Bottom) temporal clusters of microseismic events. (Top) Black circles indicate locations of microseismic events with focal mechanism solutions (see Fig. 3). Red and blue triangles indicate production and injection wells, respectively. Shaded area indicates region of San Emidio fault considered to be within the vicinity of microseismicity. (Bottom) Solid vertical lines indicate the start and stop times of the shut-in. Dashed vertical lines indicate boundaries between the three temporal groups.

Table 1
Focal mechanism qualities within each spatial and temporal cluster.

Cluster	"A" Quality	"B" Quality	"C" Quality
S1	0	0	3
S2	1	2	4
S3	0	4	2
S4	1	0	8
S5	0	0	5
T1	1	1	5
T2	1	5	8
T3	0	0	5

4. Discussion

4.1. Inferred stress states

Depending on which focal mechanisms were used in the stress inversions, there appeared to be a range of possible stress states within the reservoir. The stress inversion which used all events suggested a normal faulting environment, with a nearly vertical σ_1, and a nearly horizontal, north-south trending σ_2. This stress state is consistent with the background regional tectonic stress.

However, when focal mechanisms were clustered into spatial and

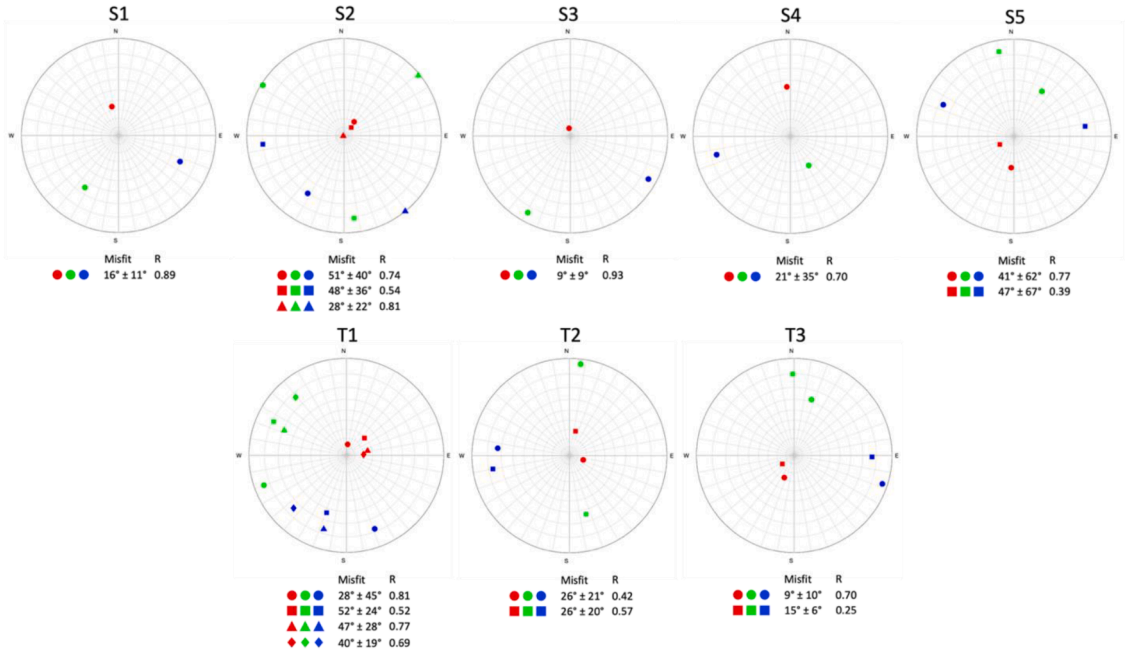

Fig. 13. Inferred principal stress directions from iterative stress inversions (Vavryčuk, 2014) for each spatial and temporal cluster of focal mechanisms. The red, green, and blue markers correspond to the inferred orientations of $\boldsymbol{\sigma}_1$, $\boldsymbol{\sigma}_2$, and $\boldsymbol{\sigma}_3$, respectively. Markers of similar shape correspond to unique inferred stress states.

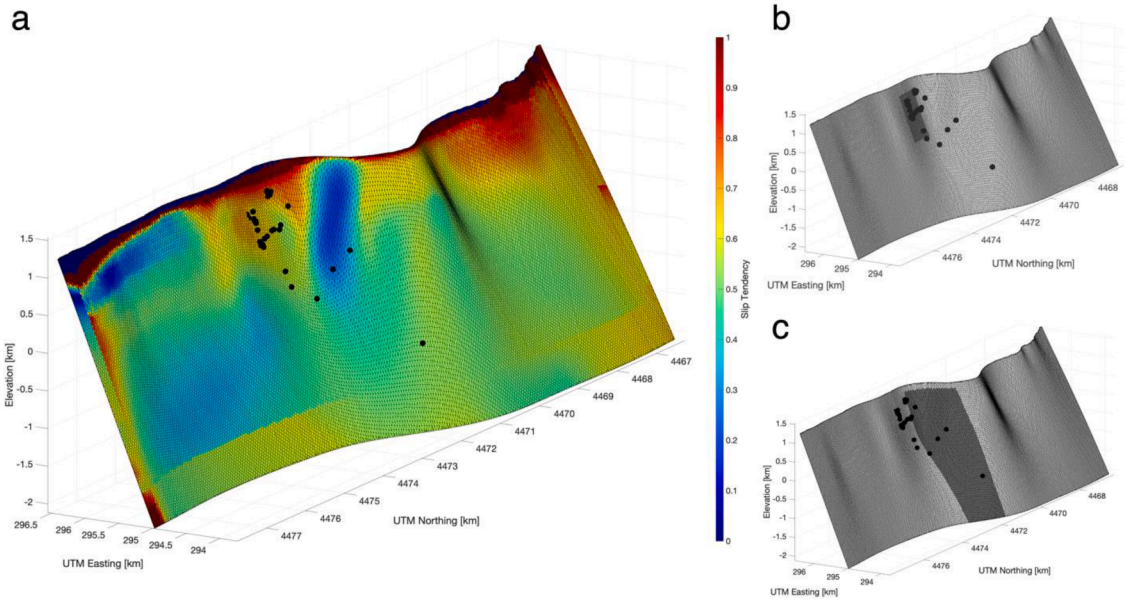

Fig. 14. Surface of San Emidio (SE) fault in the initial stress model. (a) Slip tendency projected onto SE fault from the realization of the initial stress model with an S_{Hmax} azimuth of N, and stress magnitudes $S_{Hmax} = S_{hmin}$ (stress ratio #1). Black markers indicate microseismic event locations. Warm colors indicate higher slip tendencies. Elevations are relative to mean sea level (MSL). (b) Portion of SE fault in the vicinity of microseismicity, denoted by dark gray area. (c) Portion of the SE fault in the vicinity of the kink in the fault, denoted by dark gray area.

temporal groups, multiple possibilities of stress states arose, with some stress states that were inconsistent with both the background tectonic stress and the inferred stress state when all the events were inverted. The deviation between the inferred stress states from clustered events and those from all the events may suggest that spatial and temporal stress heterogeneities exist within the reservoir. Some clusters (e.g., S3, T2, T3) are rejected by the null hypothesis of the single-sample variance test, which suggests that a single stress state may not explain the occurrence of all events within the cluster. This could indicate that there are spatial and temporal stress heterogeneities within the reservoir. The deviations could also be an artifact of the fact that some of the clusters have a very small number (<5) of events used for the stress inversions. This can increase the uncertainty of the inferred stress state. Therefore, some clusters may not contain enough focal mechanism data to be confident that the inferred stress state is actually representative of the reservoir stress state.

Slickenlines are records of slip events that occurred in the past. Therefore, an estimation of the stress state can provide insights into past stress state(s), which can then be compared to the inferred *in-situ* stress state. The inferred stress state from the slickenlines indicated a normal faulting environment with σ_2 nearly horizontal oriented N20°E, which is generally consistent with both the existing north-south striking normal fault geometry in the geothermal system and estimates of *in-situ* reservoir stress from the 2016 microseismicity.

The outcomes of the stress inversions also identify which of the two focal mechanism nodal planes most likely slipped. From the stress state inferred from all 31 focal mechanisms, the likely slip planes appear to be subparallel with the average orientation of the throughgoing faults (SE and BB faults) within the model, with some variation (Fig. 11). The cluster of inferred slip plane orientations that do not align with the model fault surfaces may be conjugate fault planes. Most of the microsesimic events are bounded by the SE and BB faults which are separated by approximately 200 m (see Fig. 1). As the width of fault damage zones can reach hundreds of meters (Choi et al., 2016), this may suggest that slip is occurring on the SE and BB faults or within a damage zone between those faults.

4.2. Stress model validation

Since slip tendency (Eq. (3)) is equivalent to the critical coefficient of friction at which fault slip should occur, slip tendencies on the faults within the model and slip tendencies on the inferred slip planes from the microsesimic focal mechanisms were used as proxies to determine the preferred realizations of the initial stress model. The majority of the microsesimic events occurred within 500 m of the Basin Bounding (BB) and San Emidio (SE) faults at depths ranging from 500 to 1500 m, therefore only those two faults were considered when evaluating each initial stress model (Fig. 14).

Four criteria were used to select preferred realizations of the initial stress model based on slip tendencies on the model faults: (1) regions of relatively high slip tendency on the model faults within the vicinity of microseismicity when compared to the fault overall, (2) absolute magnitudes of the average slip tendency on the model faults within the vicinity of microseismicity must be greater than 0.6, (3) regions of relatively high slip tendency on model faults within the vicinity of the kink in the SE fault, and (4) consistency of the initial stress model with the inferred stress states from focal mechanism and slickenline inversions. The rationale for these criteria are discussed below.

Since microseismicity from the 2016 geothermal plant shut down was confined to a relatively narrow region, a representative initial stress model should show regions of relatively high slip tendency within the vicinity of microsesimic events. If the slip tendency was lower in the vicinity of the microsesimic events than on the fault overall, then a small pore pressure change on the order of tens of kPa (Feigl et al., 2022) is unlikely to cause microseismicity. Average slip tendencies on the BB and SE faults were calculated within the vicinity of microseismicity and were then compared to the average slip tendencies on the BB and SE faults outside the vicinity of microseismicity. The zone of microseismicity was defined as the region bounded by UTM Easting coordinates between 295.85km and 296.50km, UTM Northing coordinates between 4472.35 km and 4473.20km, and elevations between −0.2km and 0.97km relative to mean sea level (MSL), corresponding to depths of about 0.26 to 1.43km (Fig. 14b). A realization of the initial stress model was determined to have relatively high slip tendency near the microseismicity if the average slip tendency on the faults within the vicinity of microseismicity was greater than the average slip tendency on the faults outside the vicinity of microseismicity.

The absolute magnitudes of slip tendency on the portions of the SE and BB faults within the vicinity of microseismicity were also evaluated. Faults are expected to slip when the slip tendency exceeds the coefficient of friction of faults. For most rock types, the coefficient of friction typically ranges between 0.6 and 0.85 (Byerlee, 1978). Since the coefficient of friction values of the reservoir rocks are unknown, we evaluated our realizations of the initial stress model using the lower bound of typical rock friction to assess the possible stress states that may reasonably describe the microseismicity. If the average slip tendency within the microseismicity was greater than 0.6, then we inferred that this portion of the fault was critically stressed, and the initial stress model produced stress magnitudes that were plausible in light of the observed microseismicity.

There is a kink in the SE fault that links the two segments of the fault together. Field observations have suggested the fault to have high permeability at this kink (Folsom et al., 2020), which implies that this section of the fault is more active when compared to the other sections of the fault (Zoback and Townend, 2001; Hennings et al., 2012). Therefore, the preferred initial stress model should have relatively high slip tendencies on the kink of the SE fault. The average slip tendency was determined on the SE fault within the bounds of the kink and then compared with the average slip tendency on the portion of the fault outside of the kink. The bounds of the kink were defined as all parts of the SE fault bounded by UTM Northing coordinates between 4471.25km and 4472.25km, and elevations less than 1.1km relative to MSL, corresponding to depths of less than about 0.13km (Fig. 14c).

The initial stress state input to the stress model should be consistent with the reservoir stress state. Guo et al. (2022) performed a bootstrapped stress inversion method using the focal mechanisms from the 2016 plant shut down, from which they inferred the S_{Hmax} azimuth to be near N10°W. Comparing these results with our own analysis using focal mechanisms from the 2016 microseismicity and slickenline data (Fig. 11 and Section 3.3.2) suggests S_{Hmax} to be oriented between N and N20°E.

The slip tendencies determined for the inferred slip planes of the focal mechanisms were greatest for realizations of the initial stress model with a transtensional stress regime and S_{Hmax} azimuths of N to N10°E. The maximum slip tendency however was 0.4, which is less than typical coefficient of friction values for crystalline, volcanic, and sedimentary rocks (Byerlee, 1978) like those at San Emidio. It is not clear whether this low slip tendency of 0.4 suggests inconsistency with our knowledge of rock friction. It is possible that the slip planes are simply weaker for instance due to the presence of clay minerals. Locally high pore pressure potentially due to the fluid flow between the injection and production wells - upon with a fluid pressure rise due to plan shut down was superimposed - may also lead to fault slip at low apparent slip tendencies. We also note that the inferred focal mechanism slip planes are not necessarily parallel to the nearby SE and BB faults (Fig. 11), and many events likely occurred within the damage zone around these faults. Even though an underlying assumption of the stress inversion is that the stress state is uniform within the volume containing the focal mechanisms, misfits exist between the predicted and actual slip directions and the inversion is only optimizing the stress state to minimize the misfit to yield an “average” stress state. Thus, it is possible that the slip planes are not necessarily optimally-oriented to the stress state recovered by the inversion, but instead are more favorably oriented (and

Table 2
Satisfied slip tendency analysis criteria on the Basin Bounding (BB) fault for all 78 realizations of the initial stress model. Blank boxes indicate no criteria was met.

BB Fault	Stress Ratio Number												
	1	2	3	4	5	6	7	8	9	10	11	12	13
S_{Hmax} Azimuth	350		R	R	R	R A	R	R		R	R		
	0		R	R	R	R A	R	R	R	R	R		
	10		R	R	R	R	R		R	R			
	20			R	R	R A	R	R					
	30		R		R	R A	R	R		R	R	R	
	40		R	R		R	R	R	R		R		A

*A: Average slip tendency on the BB fault within the vicinity of microseismicity was greater than 0.6.
**R: Average slip tendency on the BB fault within the vicinity of microseismicity eas greater than the average slip tendency on the BB fault.
***The grayed-out boxes indicate realizations of the initial stress model where all criteria was met for both faults.

Table 3
Satisfied slip tendency analysis criteria on the San Emidio (SE) fault for all 78 realizations of the initial stress model. Blank boxes indicate no criteria was met.

SE Fault		Stress Ratio Number												
		1	2	3	4	5	6	7	8	9	10	11	12	13
S_{Hmax} Azimuth	350	R A	R	R K	R	R	R			K			K	K
	0	R A	R K	R A K	A	A	R K	R K	R K	R K	R K	R K	K	K
	10	R A	R	R A	R A	R A	A	R A K	R K	R K	R K	R K	R K	R K
	20	R A	R K		R A	R A K	R A	R A K	R A K	R A K	R A K	R A	R A	R A
	30	R A	R K	R K		R A K	R A K	A	A	R A	A	R A K	R A K	R A
	40	R A		R K	R K	R K	R K			R	R	R	R K	R A

*A: Average slip tendency on the SE fault within the vicinity of microseismicity was greater than 0.6.
**R: Average slip tendency on the SE fault within the vicinity of microseismicity was greater than the average slip tendency on the SE fault.
***K: Average slip tendency on the kink of the SE fault was greater than the average slip tendency on the SE fault.
****The grayed-out boxes indicate realizations of the initial stress model where all criteria were met for both faults.

slip tendency higher) to a local stress state that slightly deviates from the average stress state. The realizations of the initial stress model account for stress heterogeneities caused by the local geology and topography to the best of our knowledge (See Section 3.2), but do not account for localized stress perturbatios due to fault zone structure or fault slip. Further information on the structural history of the region and direct borehole measurements of *in-situ* stress orientations and magnitudes, where available, would help constrain stress heterogeneities produced by these local effects and improve our interpretation.

From the slip tendencies projected onto the BB and SE faults and inferred slip planes for all 78 realizations of the initial stress model, two realizations were selected to be most plausible of the reservoir stress state based on the four criteria that were previously defined (Tables 2, 3). The two realizations have S_{Hmax} azimuths ranging between N20°E and N30°E with a stress ratio of 5 (see Fig. 5).

The average slip tendencies on the inferred slip planes from microsesimic events were greatest for the realizations of the initial stress model with S_{Hmax} azimuths of N to N10°E in a transtensional stress regime. Although not all the slip tendency analysis criteria were met for the BB and SE fault for these focal-mechanism-based realizations of the initial stress model, they should still be considered for further analysis since they describe the greatest magnitudes of slip tendencies on the inferred slip planes, yield the same stress ratios, and differ in S_{Hmax} azimuth by only 10° to 30°

5. Conclusions

The work presented used geophysical and geological data to characterize the *in-situ* stress state in the geothermal reservoir at San Emidio, Nevada, United States. These data included focal mechanisms, slickenlines, wellbore stress indicators from nearby geothermal fields, and secular strain rate measurements. The *in-situ* reservoir stress state was inferred by performing an iterative joint inversion based on a linear stress inversion using focal mechanisms from microseismic events within the reservoir that occurred during a plant shut down in 2016. The stress state was inferred to be a normal faulting environment, with σ_1 oriented nearly vertical, σ_2 oriented nearly horizontal in a north-south trending direction, and σ_3 oriented nearly horizontal in an east-west trending direction.

A set of 78 different realizations of an initial reservoir stress model were generated to explore how the slip tendency distribution in the reservoir varied with different assumptions about the azimuth of S_{Hmax} and the relative magnitudes of S_V, S_{Hmax}, and S_{hmin}. To assess the validity of the stress models, slip tendencies were calculated on the major mapped faults within the model and on the inferred slip planes of the focal mechanisms from microseismicity during the 2016 plant shut down. Realizations of the initial stress model that represent the *in-situ* reservoir stress should have regions of relatively high slip tendency on segments of the San Emidio and Basin Bounding faults nearest the microseismicity and high slip tendency on the inferred focal mechanism slip planes. This analysis favored realizations of the initial stress model with azimuths of S_{Hmax} ranging from N20°E to N30°E and relative magnitudes of S_V, S_{Hmax}, and S_{hmin} describing a transtensional stress regime, with S_{Hmax} approximately equal to S_V. Specifically, this stress model produced slip tendency distributions on the model faults that are consistent with incipient frictional failure (i.e., are critically stressed) and are most consistent with the spatial distribution of microseismicity and locations of fault segments exhibiting the greatest geothermal productivity. Realizations of the initial stress model with azimuths of S_{Hmax} ranging from N to N10°E in a transtensional stress regime produced the greatest average slip tendencies on the inferred slip planes of the microsesimic events, even though nearby segments of the San Emidio and Basin Bounding faults in this realization were not critically stressed.

CRediT authorship contribution statement

Ben Jahnke: Conceptualization, Software, Validation, Formal analysis, Data curation, Investigation, Writing – original draft, Writing – review & editing, Visualization. **Hiroki Sone:** Conceptualization, Software, Validation, Formal analysis, Data curation, Investigation, Writing – original draft, Writing – review & editing, Visualization, Supervision. **Hao Guo:** Resources, Data curation, Writing – review & editing, Visualization. **Chris Sherman:** Software, Data curation, Visualization. **Ian Warren:** Validation, Writing – review & editing. **Corné Kreemer:**

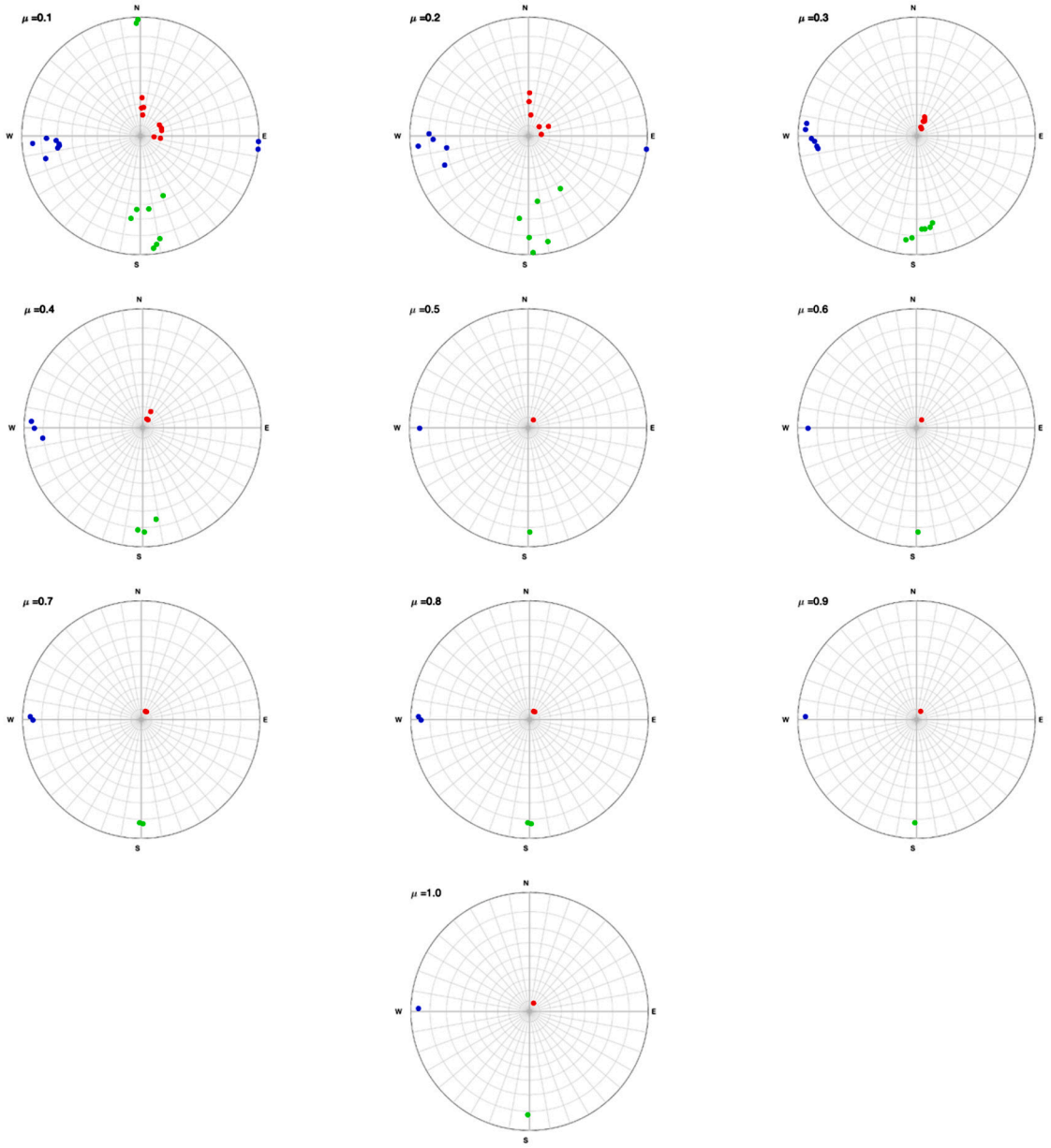

Fig. A1. : Inferred principal stress directions from the iterative stress inversion (Vavryčuk, 2014) using all focal mechanisms for coefficients of friction between 0.1 and 1. The red, green, and blue markers correspond to the inferred directions of $\boldsymbol{\sigma}_1$, $\boldsymbol{\sigma}_2$, and $\boldsymbol{\sigma}_3$, respectively.

Resources. **Clifford H. Thurber:** Resources. **Kurt L. Feigl:** Software, Validation, Formal analysis, Investigation, Data curation, Writing – original draft, Writing – review & editing, Visualization, Supervision, Project administration, Funding acquisition.

Declaration of Competing Interest

The authors declare that they have no known competing financial interests or personal relationships that could have appeared to influence the work reported in this paper.

Data availability

Data will be made available on request.

Acknowledgments

We thank Steve Hickman and the anonymous reviewer for providing feedback that helped improve the manuscript. We also thank Matt Folsom for providing the fault model and the geological map. The work presented herein has been funded in part by the Office of Energy Efficiency and Renewable Energy (EERE), U.S. Department of Energy, under Award Numbers DE-EE0007698 and DE-EE0009032.

Appendix

Fig. A1.

References

Byerlee, J., 1978. Friction of rocks. Rock Friction and Earthquake Prediction 615–626.

Choi, J.H., Edwards, P., Ko, K., Kim, Y.S., 2016. Definition and classification of fault damage zones: a review and a new methodological approach. Earth Sci. Rev. 152, 70–87, 2016.

Davatzes, N.C., Hickman, S., 2009. Fractures, stress and fluid flow prior to stimulation of well 27-15, Desert Peak, Nevada, EGS project. In: Proceedings of the 34th Workshop on Geothermal Reservoir Engineering. Stanford Univ.. Stanford, CA, SGP-TR-187.

Feigl, K.F., Tung, S., Guo, H., Cunningham, E., Hampton, J., Kleich, S.J., Jahnke, B., Heath, B., Roland, C., Folsom, M., Akerley, J., Cusini, M., Sherman, C., Warren, I., Kreemer, C., Sone, H., Cardiff, M.A., Lord, N.E., Wang, H.F., 2022. Overview and Preliminary results from the WHOLESCALE project at San Emidio, Nevada, U.S. In: Proceedings of the 47th Workshop on Geothermal Reservoir Engineering. Stanford University, Stanford, California, 7-9 February 2022.

Folsom, M., Libbey, R., Feucht, D., Warren, I., Garanzini, S., 2020. Geophysical observations and integrated conceptual models of the San Emidio geothermal field, Nevada. In: Proceedings of the 45th Workshop on Geothermal Reservoir Engineering. Stanford University, Stanford, California, 10-12 February 2020.

Guo, H., Thurber, C.H., Heath, B., Cardiff, M.A., Lord, N.E., Warren, I., & Feigl, K.L. (2022). Seismic analysis of reservoir conditions for inducing seismicity at the San Emidio geothermal field, Nevada, USA. *Abstract.* Presented at 2022 SSA Annual Meeting, Bellevue, WA, April 19-23.

Heidbach, O., Rajabi, M., Cui, X., Fuchs, K., Müller, B., Reinecker, J., Reiter, K., Tingay, M., Wenzel, F., Xie, F., Ziegler, M.O., Zoback, M.-L., Zoback, M.D., 2018. The world stress map database release 2016: crustal stress pattern across scales. Tectonophysics 744, 484–498. https://doi.org/10.1016/j.tecto.2018.07.007.

Hennings, P., Allwardt, P., Paul, P., Zahm, C., Reid, R., Alley, H., et al., 2012. Relationship between fractures, fault zones, stress, and reservoir productivity in the Suban gas field, Sumatra, Indonesia. Bulletin 96 (4), 753–772. https://doi.org/10.1306/08161109084.

Hickman, S., Davatzes, N., 2010. *In-situ* stress and fracture characterization for planning of an EGS stimulation in the Desert Peak Geothermal Field, Nevada. In: Proceedings of the 35tht Stanford Geothermal Workshop. SGP-TR-188.

Hickman, S., Zoback, M.D., Benoit, R., 1998. Tectonic controls on fault-zone permeability in a geothermal reservoir at Dixie Valley, Nevada. In: Holt, R.M. (Ed.), Proceedings of the Rock Mechanics in Petroleum Engineering, 1. Society of Petroleum Engineers, pp. 79–86.

Jaeger, J.C., Cook, N.G.W., 1971. Fundamentals of Rock Mechanics. Chapman and Hall, London.

Kreemer, C., Blewitt, G., Klein, E.C., 2014. A geodetic plate motion and global strain rate model. Geochem. Geophys. Geosyst. 15, 3849–3889. https://doi.org/10.1002/2014GC005407.

Matlick, S., 1995. San Emidio geothermal system, Empire, NV. GRC Field Trip – October. Mesquite Group, Inc, 1995.

Michael, A.J., 1984. Determination of stress from slip data: faults and folds. J. Geophys. Res. 89, 11, 517–11,526.

Morris, A., Ferill, D.A., Henderson, D.B., 1996. Slip tendency analysis and fault reactivation. Geology 24, 275–278.

Settgast, R.R., White, J.A., Corbett, B.C., Vargas, A., Sherman, C., Fu, P., Annavarapu, C., & USDOE National Nuclear Security Administration. (2018). GEOSX simulation framework [Computer software. https://www.osti.gov//servlets/purl/1422506. 10.11578/dc.20201028.2.

Siler, D.L., Faulds, J.E., Mayhew, B., and Mcnamara, D.D., 2016, Geothermics Analysis of the favorability for geothermal fluid flow in 3D: astor pass geothermal prospect, Great Basin, northwestern Nevada, USA: geothermics, v. 60, p. 1–12, doi:10.1016/j.geothermics.2015.11.002.

Rhodes, G.T., 2011. Structural Controls of the San Emidio Geothermal System, Northwestern Nevada. Unversity of Nevada, Reno]. University of Nevada [Master's DissertationReno ScholarWorks Repository.

Rhodes, G.T., Faulds, J.E., & Ramelli, A.R. (2011) Preliminary geologic map of the Northern Lake Range, San Emidio Geothermal Area, Washoe County, Nevada. Nevada Bureau of Mines and Geology, Open-File report, 11-11.

Theis, C.V., 1940. The source of water derived from wells: essential factors controlling the response of an aquifer to development. Civ. Eng. 10 (5), 277–280.

Vavryčuk, V., 2014. Iterative joint inversion for stress and fault orientations from focal mechanisms. Geophys. J. Int. 199, 69–77. https://doi.org/10.1093/gji/ggu224.

Warren, I., E. Gasperikova, and S. Pullammanappallil (2019), Final phase 1 report DE-EE0007698: a novel approach to map permeability using passive seismic emission tomography. https://subterraseis.com/wp-content/uploads/2019/10/Doc1.pdf.

Zoback, M.D., 2007. Reservoir Geomechanics. Cambridge University Press, New York, NY, USA, p. 449.

Zoback, M.D., Harjes, H.-P., 1997. Injection-induced earthquakes and crustal stress at 9km depth at the KTB deep drilling site, Germany. J. Geophys. Res. 102 (B8), 18477–18491. https://doi.org/10.1029/96JB02814.

Zoback, M., Townend, J., 2001. Implications of hydrostatic pore pressures and high crustal strength for the deformation of intraplate lithosphere. Tectonophysics 336, 19–30. https://doi.org/10.1016/s0040-1951(01)00091-9.

Zoback, M.L., "State of stress and modern deformation of the Northern Basin and Range Province" (1989). USGS Staff – Published Research. 459.